Bone 127 (2019) 120–128

Contents lists available at ScienceDirect

Bone

journal homepage: www.elsevier.com/locate/bone

Full Length Article

Volumetric mapping of bound and pore water as well as collagen protons in cortical bone using 3D ultrashort echo time cones MR imaging techniques

Saeed Jerban[a,1], Yajun Ma[a,1], Liang Li[a], Hyungseok Jang[a], Lidi Wan[a], Tan Guo[a], Adam Searleman[a], Eric Y. Chang[b,a], Jiang Du[a,*]

[a] Department of Radiology, University of California, San Diego, CA, USA
[b] Radiology Service, VA San Diego Healthcare System, San Diego, CA, USA

ARTICLE INFO

Keywords:
Cortical bone
MRI
Ultrashort echo time
Collagen proton density
Magnetization transfer
Pore water

ABSTRACT

Cortical bone assessment using magnetic resonance imaging (MRI) has recently received great attention in an effort to avoid the potential harm associated with ionizing radiation-based techniques. Ultrashort echo time MRI (UTE-MRI) techniques can acquire signal from major hydrogen proton pools in cortical bone, including bound and pore water, as well as from the collagen matrix. This study aimed to develop and evaluate the feasibility of a technique for mapping bound water, pore water, and collagen proton densities in human cortical bone *ex vivo* and *in vivo* using three-dimensional UTE Cones (3D-UTE-Cones) MRI. Eight human tibial cortical bone specimens (63 ± 19 years old) were scanned using 3D-UTE-Cones sequences on a clinical 3 T MRI scanner and a micro-computed tomography (μCT) scanner. Total, bound, and pore water proton densities (TWPD, BWPD, and PWPD, respectively) were measured using UTE and inversion recovery UTE (IR-UTE) imaging techniques. Macromolecular proton density (MMPD), a collagen representation, was measured using TWPD and macromolecular fraction (MMF) obtained from two-pool UTE magnetization transfer (UTE-MT) modeling. The correlations between proton densities and μCT-based measures were investigated. The 3D-UTE-Cones techniques were further applied on ten young healthy (34 ± 3 years old) and five old (78 ± 6 years old) female volunteers to evaluate the techniques' feasibility for translational clinical applications. In the *ex vivo* study, PWPD showed the highest correlations with bone porosity and bone mineral density (BMD) ($R = 0.79$ and -0.70, $p < 0.01$). MMPD demonstrated moderate to strong correlations with bone porosity and BMD ($R = -0.67$ and 0.65, $p < 0.01$). MMPD showed strong correlation with age in specimens from female donors ($R = -0.91$, $p = 0.03$, $n = 5$). The presented comprehensive 3D-UTE-Cones imaging protocol allows quantitative mapping of protons in major pools of cortical bone *ex vivo* and *in vivo*. PWPD and MMPD can serve as potential novel biomarkers to assess bone matrix and microstructure, as well as bone age- or injury-related variations.

1. Introduction

Cortical bone assessment using magnetic resonance imaging (MRI) has recently received great attention in an effort to avoid the potential harms associated with ionizing radiation-based techniques and to investigate the bone's organic matrix [1–8]. Notably, clinical MRI sequences are not employed for cortical bone imaging because they are not capable of detecting considerable signal from cortical bone [1,2]. The detected signal intensity of a tissue in MR imaging depends on various factors, including apparent transverse relaxation time (T2*), which is very short in bone [1,2]. Ultrashort echo time (UTE) MRI can image cortical bone [1–8]. By employing UTE-MRI techniques, the signal can be acquired a few microseconds after radiofrequency (RF) excitation before a major decay in transverse magnetization.

At least three hydrogen proton pools with different T2* values are present in bone: 1) collagen backbone, or macromolecular, protons, 2) bound water (BW) protons, and 3) pore water (PW) protons [2,5,9–11]. The associated T2* values for the aforementioned proton pools on a 3 T

Abbreviations: MR, magnetic resonance; MRI, magnetic resonance imaging; 3D-UTE, three-dimensional ultrashort echo time imaging; RF, radio frequency; FOV, field of view; MT, magnetization transfer; ROI, region of interest; TE, echo time; TR, repetition time; μCT, micro computed tomography; MMF, macromolecules fraction; $T2_{MM}$, macromolecular T2; FA, flip angle; BMD, bone mineral density; BWPD, bound water proton density; PWPD, pore water proton density; TWPD, total water proton density; MMPD, macromolecular proton density; PBS, phosphate buffered saline

* Corresponding author at: Department of Radiology, University of California, 9500 Gilman Drive, San Diego, CA 92093, USA.
E-mail address: jiangdu@ucsd.edu (J. Du).

[1] The first two authors made equal contributions.

https://doi.org/10.1016/j.bone.2019.05.038
Received 6 March 2019; Received in revised form 28 May 2019; Accepted 31 May 2019
Available online 05 June 2019

MR scanner are < 20 μs, 300–400 μs, and > 1 ms, respectively [1,2,5]. BW content correlates positively with the bone's mechanical properties, while PW content correlates negatively with bone's mechanical properties [8,12,13]. The content of macromolecular protons is assumed to be correlated with bone's mechanical [14] and microstructural [15] properties. The T2* of collagen backbone protons is extremely short; therefore, they cannot be directly imaged with UTE sequences on current MRI scanners.

Total water proton density (TWPD) in cortical bone can be estimated by comparing the UTE-MRI signal in cortical bone against an external reference of known water content [5,10,16–20]. The external reference is often a mixture of distilled water and heavy water (*e.g.*, 20% H2O and 80% D2O) doped with $MnCl_2$ and titrated to match the effective T2* of cortical bone. BW proton density (BWPD) in cortical bone has been estimated by comparing the inversion recovery UTE-MRI (IR-UTE-MRI) signal in cortical bone against an external reference [5, 10, 20, 21]. PW proton density (PWPD) can be estimated indirectly by subtracting BWPD from TWPD in cortical bone [17,22]. In an alternative approach, PWPD can also be estimated using a double adiabatic full passage pulse (DAFP) preparation to saturate the BW signal, followed by UTE acquisition to selectively detect signal from PW [10,20,23,24].

Magnetization transfer (MT) imaging combined with UTE-MRI has recently been used to indirectly measure the collagen protons' fraction in bone [25–28]. In UTE-MT, a high-power saturation RF pulse is used with a pre-defined series of frequency offsets from the water protons' resonance frequency to saturate protons mainly in the macromolecular matrix (namely, collagen backbone protons). The saturated magnetization transfers from protons in macromolecules to water protons, which can then be detected by UTE-MRI. The two-pool model employs UTE-MT data acquired with a series of frequency offsets and MT powers to estimate the macromolecular proton fraction (MMF) and relaxation time, as well as exchange rates. MMF may differ by variations of both collagen protons and water protons, which, in turn, complicates the cross-sectional or longitudinal comparisons. The macromolecular proton density (MMPD) as an absolute measurement of the collagenous matrix can be estimated using the MMF derived from UTE-MT modeling and the TWPD derived from UTE imaging.

The main objective of this study was to develop a comprehensive 3D UTE imaging protocol for volumetric mapping of all the major hydrogen proton pools in bone presented as BWPD, PWPD, TWPD, and MMPD. These proton maps were generated *ex vivo* and *in vivo* in human tibial cortical bone. Such comprehensive proton density mapping could potentially be used to estimate the bone fracture risk in patients.

2. Materials and methods

2.1. Ex vivo proton density mapping

2.1.1. Specimen preparation

Eight cortical bone specimens were harvested from freshly frozen human tibial midshafts (63 ± 19 years old, 5 women, 3 men), provided by a non-profit whole-body donation company (United Tissue Network, AZ, USA). Bone specimens were cut to 30 mm in length using a commercial band saw. All bone specimens were immersed in phosphate-buffered saline (PBS) for 4 h at room temperature before the MRI scans. Loose marrow, which was not trapped in pores, was removed with a scalpel in order to avoid fat floating during the scans, where the bone specimens were placed in a plastic container filled with perfluoropolyether (Fomblin, Ausimont, NJ, USA) to minimize dehydration and susceptibility artifacts.

2.1.2. UTE-MR imaging

The UTE-MRI scans were performed on a 3T MRI (MR750, GE Healthcare Technologies, WI, USA) scanner using an eight-channel knee coil for both RF transmission and signal reception. Absolute proton density measurement in bone was performed through MRI signal comparison between bone and an external reference of known proton density (20% volume H_2O, 80% volume D2O, doped with 24 mmol/L $MnCl_2$, 22 mol/L H^1, T2 ≈ 0.35 ms, T1 ≈ 6 ms). Theory and required equations to calculate the proton densities are given in Appendix I. To measure TWPD, BWPD, and PWPD, the following imaging protocols were performed to acquire UTE and IR-UTE images: A) a PD-weighted 3D-UTE-Cones sequence (TR = 100 ms, TE = 0.032 ms, FA = 10°, rectangular RF pulse of 26 μs) for TWPD measurement with 3.5 min scan time, B) a 3D-IR-UTE-Cones sequence (TR = 100 ms, TI = 45 ms, TE = 0.032 ms, FA = 20°, rectangular RF pulse of 56 μs) for BWPD measurement with 3.5 min scan time. $T_{1\text{-BW}}$ was set to 135 ms for BWPD measurement, as previously measured for eight volunteers [29]. To measure $T_{1\text{-TW}}$ as a prerequisite for the two-pool MT modeling, an actual flip angle-variable TR (AFI-VTR)-based 3D-UTE-Cones sequence (AFI: TE = 0.032 ms; TRs = 20 ms and 100 ms; FA = 45°; VTR: TE = 0.032 ms; TRs = 20, 30, 50, and 100 ms; FA = 45°, rectangular RF pulse with a duration of 150 μs) was performed with a total scan time of 20 min [30]. The scan time for B1 mapping, TR-20, TR-30, TR-50, and TR-100 ms sequences were 7, 1, 1.5, 3.5, and 7 min, respectively. Additionally, a 3D-UTE-Cones-MT sequence (Fermi saturation pulse power = 500°, 1000°, and 1500°; frequency offset = 2, 5, 10, 20, and 50 kHz; FA = 7°; 9 spokes per MT preparation; rectangular RF excitation pulse of 100 μs) was performed for two-pool MT modeling with a total scan time of 14 min (MT sequence duration < 1 min) [31–33]. Field of view (FOV), matrix dimension, nominal in-plane pixel size, and slice thickness were 14 cm, 160 × 160, 0.87 mm, and 2 mm, respectively. At the end, a large homogenous water phantom was imaged using the UTE-MRI protocol to generate the coil sensitivity map (η) over the selected FOV.

2.1.3. MRI data analysis and proton density assessment

$T_{1\text{-TW}}$ pixel maps were generated based on single-component exponential fittings on the acquired Cones-AFI-VTR data [30]. MMF pixel maps were generated from the acquired MT data using the two-pool MT model. TWPD, BWPD, PWPD, and MMPD pixel maps were generated based on the acquired pixel maps of T1 and MMF, as described in Appendix I using a set of in-house codes developed in MATLAB (version 2017, Mathworks, MA, USA). All maps were smoothed using a Gaussian filter with a 4 × 4 sub-window.

2.1.4. Micro-computed tomography (μCT)

To validate the *ex vivo* results, the calculated proton densities were compared with intracortical bone porosity (Ct.Po) and mineral density (BMD), which were measured with microcomputed tomography (μCT). All specimens were scanned using a Skyscan 1076 (Kontich, Belgium) μCT scanner at 9 μm isotropic voxel size. For BMD assessment, specimens were scanned in the presence of two hydroxyapatite phantoms (0.25 and 0.5 g/cm^3). Other scanning parameters were as follows: a 0.05 mm aluminum plus 0.038 mm copper filter, 100 kV, 100 mA, 0.4° rotation step, and 5 frame-averaging.

Fig. 1 shows selected 3D-UTE-Cones and IR-UTE-Cones imaging of an *ex vivo* tibial bone specimen from a 73-year-old male donor. One of the corresponding μCT images to the selected MRI slice is also shown in Fig. 1c. An external water phantom (20% volume H2O) was placed in the middle of the bone sample.

A single gray level threshold was used for μCT image segmentation to distinguish between bone and pores. The threshold was selected for each dataset based on the two major peaks of gray level histograms and visual inspection of the raw images. Thresholding resulted in a stack of binary images. Ct.Po and BMD pixel maps were generated for each specimen by superimposing 222 binary images corresponding to a 2-mm MRI slice.

2.1.5. MRI and μCT correlations

Proton densities from MRI analyses were compared with Ct.Po and

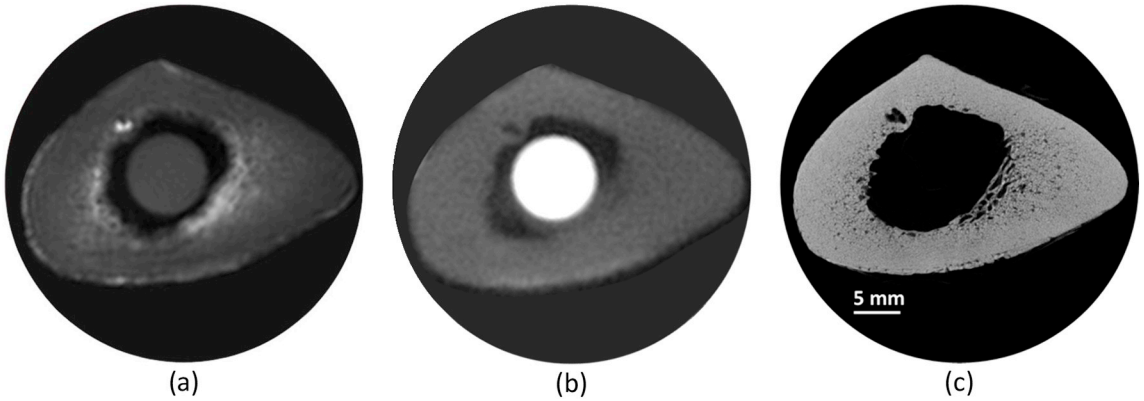

Fig. 1. Representative (a) 3D-UTE-Cones and (b) IR-UTE-Cones imaging, as well as (c) μCT imaging of an *ex vivo* tibial cortical bone specimen (73-year-old male). A water calibration phantom was placed in the middle of the bone sample for measurement of water and collagen proton densities.

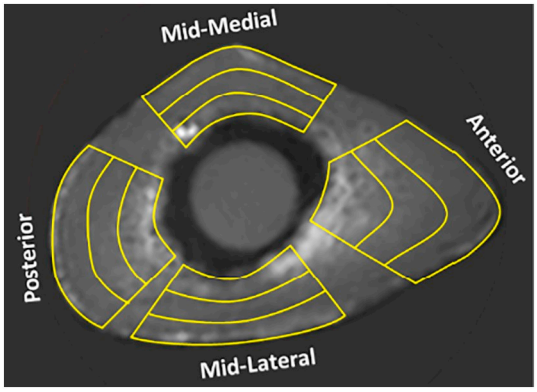

Fig. 2. Schematic representation of the selected ROIs for *ex vivo* bone specimens (3 cortical layers and 4 anatomical locations).

BMD within twelve regions of interest (ROIs) per specimen. Fig. 2 shows the twelve selected ROIs schematically in a representative tibial sample. ROIs were organized to capture anterior/posterior and medial/lateral quadrants as well as periosteal, intracortical, and endosteal layers of the cortex (Fig. 2). This ROI selection provided an adequate range of Ct.Po and BMD.

Affine image registration was used to register the selected UTE-MRI slice from each bone specimen to the corresponding generated μCT-based porosity map. Four pairs of identical points were manually selected in both UTE-MRI slice and μCT-based porosity map by a medical imaging expert to calculate a 2D transformation matrix. The transformation matrix was used to map the ROIs used for MRI analysis on the μCT data. All the data analyses were performed in MATLAB (version 2017, The Mathworks Inc., Natick, MA, USA). Pearson's correlations were calculated between proton densities and μCT-based measures using MATLAB. All ROIs were considered together in statistical correlations in order to examine the UTE-MRI method's capability to detect the variation of bone microstructure regardless of the intracortical bone location. While this does introduce some interdependency between data points, significance levels for all correlations were assessed using non-parametric bootstrap (with resampling by specimen) to adjust for within-specimen dependence. Afterwards, a series of mixed-effects linear regression models (multi-variable linear regressions) were performed to find out how porosity or BMD can be predicted by each one of the proton densities (BWPD, PWPD, TWPD, and MMPD) in the presence of others. In each model, porosity or BMD was considered as the outcome while a combination of proton densities was considered as the predictor. An optimal model for each outcome was selected based on Akaike Information Criterion. Since TWPD was BWPD + PWPD, the combination of the three was not considered in the models. For each outcome (*i.e.*, porosity and BMD), the following two models were developed: first, TWPD combined with MMPD and second, BWPD and PWPD combined with MMPD. Statistical analyses were performed using a statistical programming language (R, version 3.2.5, R Development Core Team, Vienna, Austria).

2.2. *In vivo* proton density mapping

Tibial midshafts in ten young healthy (34 ± 3 years old) and five old (78 ± 6 years old) female volunteers were imaged using the same RF coil and sequences described for *ex vivo* studies. All *in vivo* studies were performed with institutional review board approval and written informed consent. Female volunteers were recruited through local advertisement. Pregnant women and unhealthy volunteers were excluded after an initial screening questionnaire. The imaging slab was centered at the tibial midshaft localized based on the operator experience. MRI sequences for *in vivo* imaging were similar to *ex vivo* imaging, but with higher slice thickness (5 mm) to improve the signal to noise ratio (SNR).

To investigate the reproducibility level of the developed comprehensive technique, the lower leg of a healthy male volunteer subject (37-year-old male) was scanned three times at different time points. In addition to qualitative comparisons, the average, standard deviation, and coefficient of variation of MMF and proton densities from the three scans were compared.

3. Results

Fig. 3 illustrates sequential steps of the developed method for generating 3D proton density maps for a representative *ex vivo* tibial specimen. Volumetric $T_{1\text{-TW}}$ map from AFI-VTR technique and MMF map from two-pool MT modeling are shown in Fig. 3a and b, respectively. Fig. 3c–e illustrate the TWPD, BWPD, and PWPD maps generated from 3D-UTE-Cones and IR-UTE-Cones images. MMPD map generated by combining TWPD and MMF is shown in Fig. 3f. Ct.Po and BMD maps generated from corresponding 222 μCT images are illustrated in Fig. 3g and h, respectively.

Table 1 presents the Pearson's correlations, 95% confidence intervals, and *p*-values between obtained proton densities and μCT-based measures for 96 ROIs in total. Significance for all correlations was assessed using non-parametric bootstrap (with resampling by specimen) to adjust for within-specimen dependence. Ct.Po and BMD demonstrated the highest correlation with PWPD ($R = 0.79$ and $R = 0.70$, $p < 0.01$). Results of the mixed-effects linear regression models showed that all proton densities were correlated significantly ($p < 0.01$) with both μCT-based outcomes (*i.e.*, porosity and BMD) using both developed multi-variable regression models (TWPD + MMPD or BWPD + PWPD + MMPD). This means that all proton densities were independent predictors of porosity and BMD.

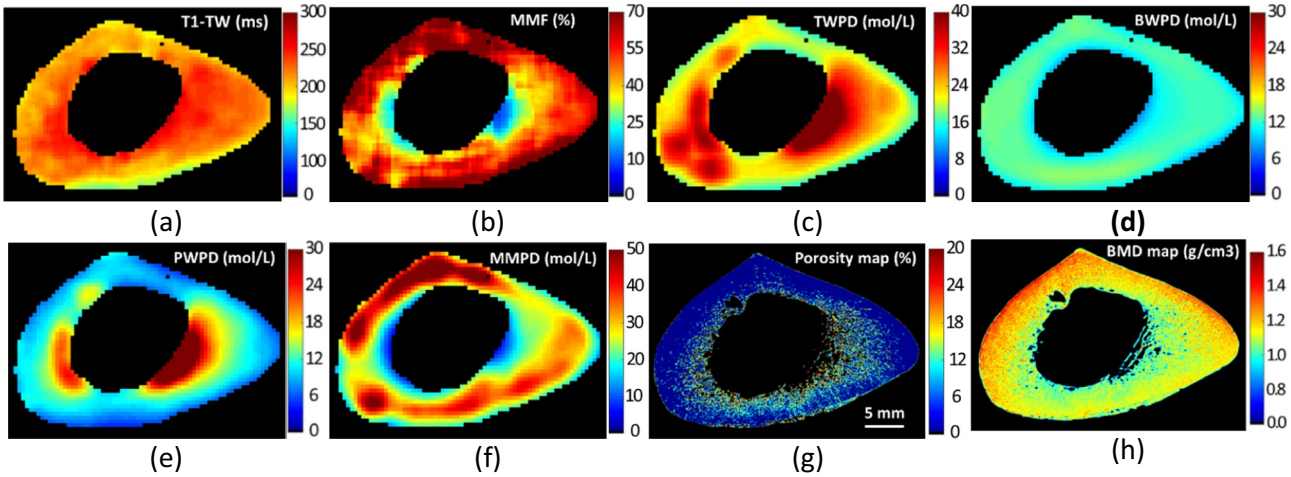

Fig. 3. Various steps involved in the developed volumetric proton density mapping method for a representative bone specimen. (a) Total water T1 map (T1-TW) derived from 3D UTE-Cones-AFI-VTR imaging. (b) Macromolecular fraction (MMF) map obtained from two-pool MT modeling of 3D UTE-Cones-MT imaging. (c) Total water proton density (TWPD) map obtained from PD-weighted 3D UTE-Cones imaging, (d) bound water proton density (BWPD) map derived from 3D IR-UTE-Cones imaging, (e) pore water proton density (PWPD) map derived from the subtraction of TWPD and BWPD, and (f) macromolecular proton density (MMPD) derived from the multiplication of TWPD and MMF. For comparison, (g) bone porosity and (h) mineral density maps were also generated for 222 corresponding μCT images.

Table 1
Pearson's correlations (shown as bold), 95% confidence intervals, and *p* values between proton densities and μCT results in eight *ex vivo* tibial cortex (96 ROIs). Significance levels for all correlations were assessed using non-parametric bootstrap (with resampling by specimen) to adjust for within-specimen dependence.

	TWPD	BWPD	PWPD	MMPD
Ct.Po	**0.73**	**−0.22**	**0.79**	**−0.67**
	[0.59,0.86]	[−0.40,0.16]	[0.62,0.89]	[−0.77,−0.55]
	$p < 0.01$	$p = 0.08$	$p < 0.01$	$p < 0.01$
BMD	**−0.65**	**0.15**	**−0.70**	**0.65**
	[−0.82,−0.46]	[−0.12,0.44]	[−0.86,−0.53]	[0.51,0.74]
	$p < 0.01$	$p = 0.09$	$p < 0.01$	$p < 0.01$

BPO: bone porosity, BMD: bone mineral density. TWPD, BWPD, PWPD, and MMPD: total water, bound water, pore water, and macromolecular proton densities, respectively.

Fig. 4a–d demonstrate the scatter plots and the linear regression analyses of estimated proton densities, including TWPD, BWPD, PWPD, and MMPD *versus* the μCT-based bone porosity. While BWPD showed little correlation with BPO, other investigated proton densities showed strong correlations with BPO, with R ranging from 0.67 to 0.79 and $p < 0.01$.

Fig. 5 shows the generated proton density maps and corresponding μCT images in four bone specimens from female donors with various ages at death (*i.e.*, 45, 49, 86, and 95 years old). First to fifth rows of subfigures show MMF, TWPD, BWPD, PWPD, and MMPD maps, respectively. The sixth row shows the corresponding μCT images scanned at 9 μm voxel size for the selected donors. Local maxima of PWPD corresponded to higher porosities and large pores presented in μCT images. This indicates strong correlation between PWPD and Ct.Po, as presented in Table 1 and Fig. 4. PWPD was slightly higher on average for the older bone specimens ($R = 0.43$, $p = 0.47$). MMPD was obviously lower for bone specimens from elderly donors. Considering all eight studied bone specimens, average MMPD was found to be moderately correlated ($R = 0.58$, $p = 0.13$) with age. MMPD and age correlation was much stronger ($R = 0.91$, $p = 0.03$) when counting only the limited female specimens ($n = 5$).

Fig. 6 shows the generated proton density maps for two young healthy (33 and 36 years old) and two old (75 and 76 years old) female volunteers. First to fifth rows of subfigures show MMF, TWPD, BWPD, PWPD, and MMPD maps, respectively. Qualitatively, PWPD appeared higher in older individuals compared with younger individuals. However, BWPD and MMPD were lower for older individuals.

Table 2 presents the average proton densities from *ex vivo* ($n = 8$), young *in vivo* ($n = 10$), and old *in vivo* ($n = 5$) studies. On average, TWPD and PWPD were higher for old individuals compared with the young groups and the *ex vivo* scans. Conversely, BWPD and MMPD were lower for the old group compared with the young group and *ex vivo* study.

Reproducibility investigation results of the developed technique performed on a healthy subject (37-year-old male) are presented in Supplemental Table 1 and Supplemental Fig. 1. The average coefficients of variation (*i.e.*, standard deviation/average) for MMF, TWPD, BWPD, PWPD, and MMPD of the healthy volunteer on three repeated acquisitions were 1.0, 2.3, 3.0, 1.9, and 2.5%, respectively.

4. Discussion

This study focused on generating proton density maps for bound and pore water pools as well as for collagen matrix of cortical bone. Density maps of protons in macromolecules (*i.e.*, MMPD) were presented for the first time in this study by combining the two-pool 3D-UTE-Cones-MT modeling [26,27,34] and TWPD measured using PD-weighted 3D-UTE-Cones imaging. MMPD mapping can be potentially used to localize bone injury and weak spots in the bone matrix that are prone to fracture. It is assumed that MMPD represents the bone collagenous matrix spatial distribution and that it potentially correlates with the bone's viscoelastic properties, such as mechanical toughness. Parameters of UTE-MT technique have demonstrated good correlation with human bone porosity [15,25].

The accurate estimation of bone water protons requires the consideration of i) different relaxation times between cortical bone and the reference water phantom, ii) variation in coil sensitivity, and iii) RF pulse duration and inhomogeneity (or actual flip angles) [17]. Due to short $T_{1\text{-}TW}$ in cortical bone and to the use of a relatively low FA and relatively high TR in the PD-weighted 3D-UTE-Cones sequence, the T1 effect on the TWPD calculation could be neglected. Because the T2*s of the external water phantom and bone were similar and because of the use of an ultrashort TE of 32 μs, the T2* term in the proton density measurement could also be neglected (Eq. (1)). The IR-UTE signal in cortical bone is typically uniform and smooth; therefore, using a

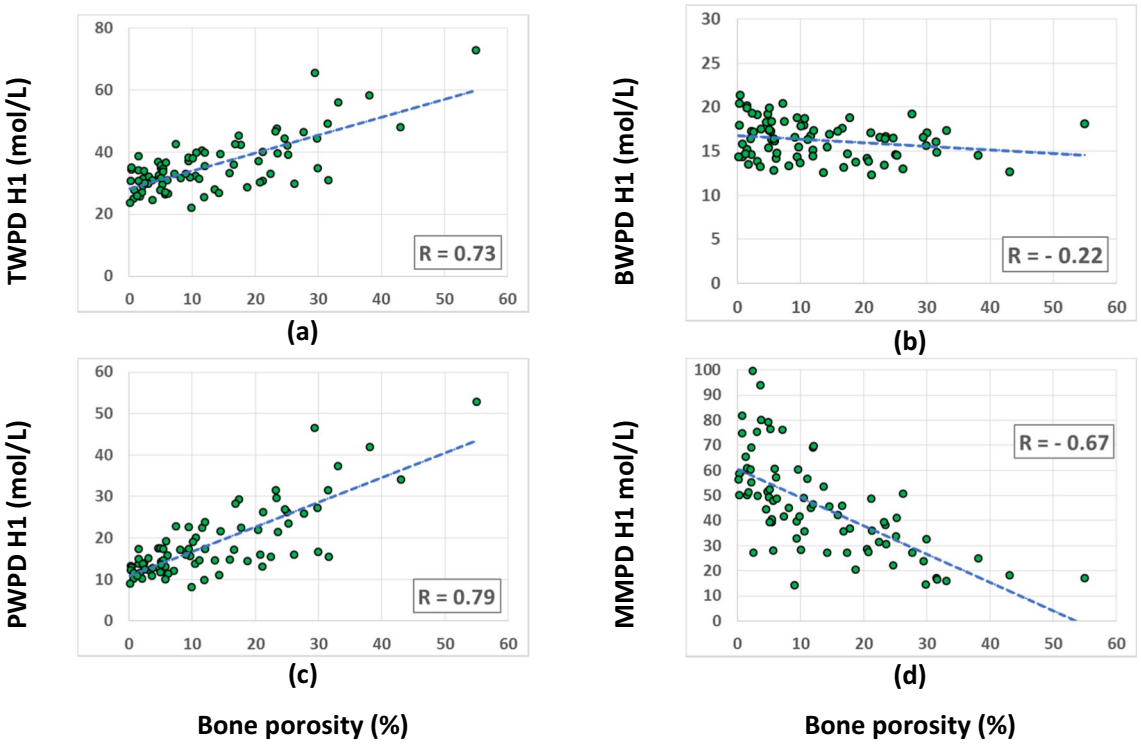

Fig. 4. Scatter plots and linear regression analyses of proton densities and bone porosity (BPO) measured for 96 ROIs from eight bone specimens. (a) Total water proton density (TWPD), (b) bound water proton density (BWPD), (c) pore water proton density (PWPD), and (d) macromolecular proton density (MMPD) *versus* μCT-based BPO.

constant value for $T_{1\text{-BW}}$ based on the literature was assumed to be practical and accurate ($T_{1\text{-BW}}$ = 135 ms). For accurate $T_{1\text{-TW}}$ measurement required for MT modeling, the B1 inhomogeneity was corrected to consider the actual FA instead of the nominal FA [30]. Utilizing such pixel maps, rather than the constant values from the literature [2,5,10,16–20], will enable more accurate localization of bone matrix variation using MMPD in future translational and longitudinal studies. Furthermore, cortical bone T1 varies significantly between subjects [35], as well as between different bone sites within certain subjects depending on the bone porosity.

Investigating 96 ROIs from eight specimens revealed significant statistical correlations between μCT-based microstructural measures and proton densities. As expected, bone porosity revealed strong correlation with PWPD (Table 1, Fig. 4). The PWPD and TWPD correlations with μCT porosity were higher than reported values in previous studies [8,13,19]. PWPD showed slightly higher values on average for the two older bone specimens (Fig. 5). Interestingly, MMPD demonstrated more significant differences between the young and old female donors (Fig. 5). Remarkably, MMPD and age correlation was strong within bone specimens from female donors (R = 0.91, p = 0.03), even though a limited number of specimens was analyzed (n = 5). Such a high correlation may weaken when investigating a higher number of specimens.

To investigate the feasibility of the techniques and to initiate the techniques' translation to clinical studies, ten young healthy and five old female volunteers were scanned using the same 3D-UTE-Cones MRI sequences and RF coil. For *In vivo* scans, the slice thickness was higher to provide adequate SNR in images. On average, TWPD and PWPD were higher for old individuals compared with the young group (Table 2). However, MMPD was lower for the old group compared with young group and the *ex vivo* study. BWPD did not show reasonable variation between the studied groups. It should be noted that the reproducibility study performed on a healthy volunteer subject showed slight variations in estimated MMF and proton densities (≤3% variation coefficient, Supplemental Figure1 and Supplemental Table 1).

The ratio between BWPD to PWPD in this study was lower than the reported values in previous studies for tibia [10,20]. Higher BWPD may have resulted from high $T_{1\text{-BW}}$ values (290 ms) used in previous studies. In the current study, $T_{1\text{-BW}}$ was set to 135 ms based on eight previously scanned subjects [29].

This study enriches the bone imaging literature currently focused on MRI-based proton density mapping in cortical bone [2,5,10,16–19,23]. Here, the technique for mapping MMPD is presented for the first time as a potentially crucial tool for evaluating bone matrix and as a potentially sensitive and novel biomarker of aging. Incorporating the MMPD mapping in cortical bone to the current imaging standard may provide a more comprehensive tool for future bone disease evaluation. Further, the use of 3D-UTE-Cones sequences greatly facilitates translational studies due to the much higher efficiency of Cones trajectories over 2D or 3D radial trajectories in sampling k-space data.

MMPD mapping presented in this study may need further *ex vivo* validation using Fourier-transform infrared spectroscopy (FTIR) or Raman spectroscopy (RS) techniques. FTIR and RS detect the vibration characteristics of chemical bonds in molecules. In FTIR technique, the collagen chemical bonds fractions in a specimen can be estimated based on their absorption level of infrared radiation in a specific wavelength (cm^{-1}) range [36]. In RS technique, near-infrared light beams are utilized to exploit the inelastic scattering phenomena of the light beams, where the level of shifted energy in the scattered beams is indicative of discrete vibrational modes, which is specific for collagen chemical bonds and leads to an estimation of collagen fraction [37]. FTIR and RS have shown potential for mapping spatial collagen distribution in tissue specimens, even though they are limited to a low penetration depth and they require direct exposure to the specimens [36,38–41].

This study has several limitations. First, while the presented techniques were translated to *in vivo* applications, only a limited number of healthy and old volunteers were recruited for this feasibility study. The

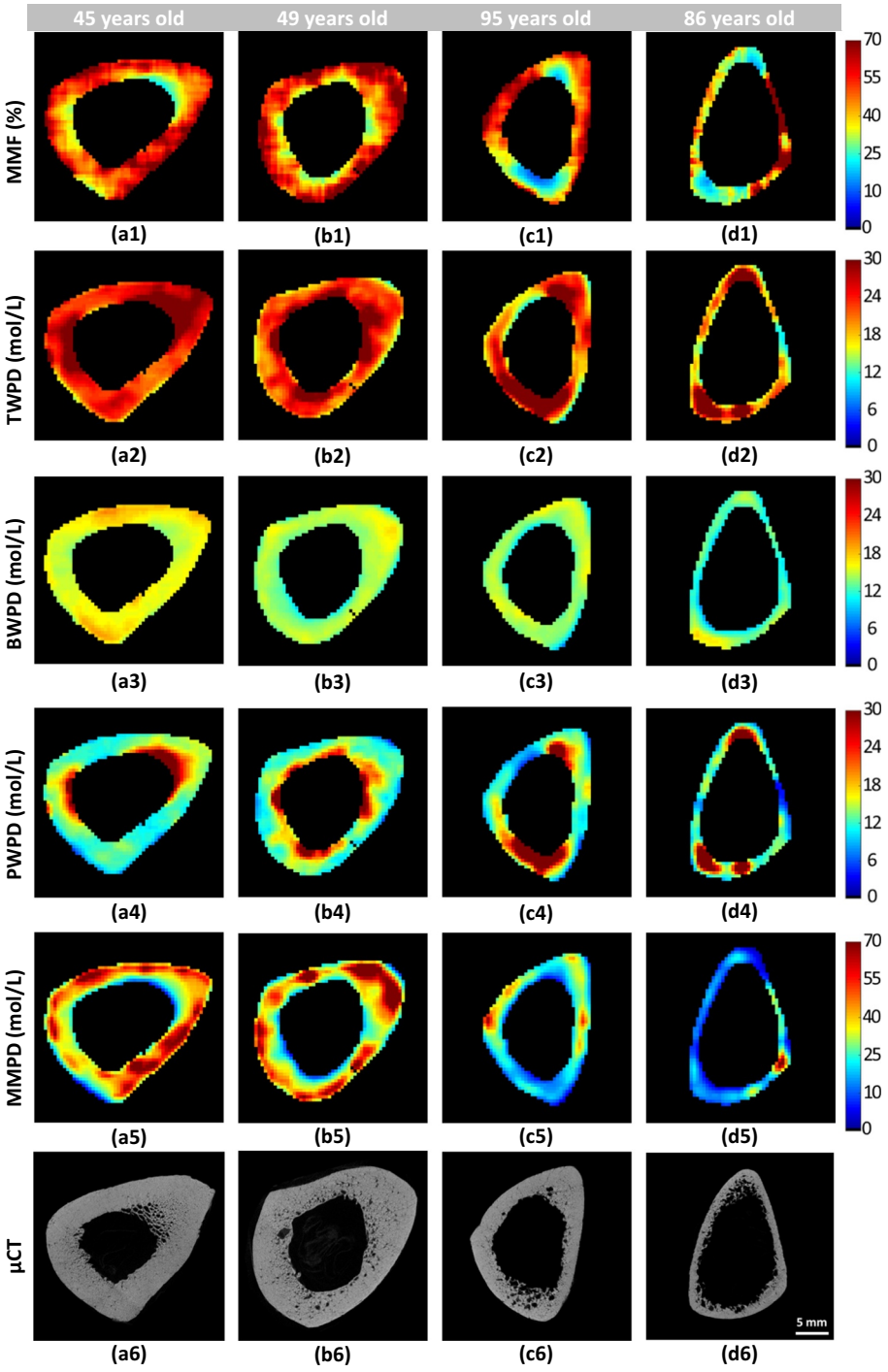

Fig. 5. Generated proton density maps and corresponding selected µCT images of four bone specimens from female donors with various ages at death; (a1-a6) 45, (b1-b6) 49, (c1-c6) 95, and (d1-d6) 86 years old. (a1-d1) macromolecular fraction (MMF) derived from 3D UTE-Cones-MT modeling. (a2-d2) total water proton density (TWPD) maps calculated from PD-weighed 3D UTE-Cones imaging. (a3-d3) bound water proton density (BWPD) maps calculated from 3D IR-UTE-Cones imaging. (a4-d4) pore water proton density (PWPD) maps derived from subtraction of TWPD from BWPD. (a5-d5) macromolecular proton density (MMPD) maps derived from TWPD combined with MMF. (a6-d6) corresponding µCT images of the four studied specimens. Local maxima in PWPD correspond to the sites of higher porosities in µCT images. MMPD in older specimens were significantly lower.

techniques and the protocol need to be examined on a larger cohort of volunteers, especially in patients with osteoporosis and other bone diseases, in order to demonstrate their capability in distinguishing between normal and weakened bone. Second, the total scan time was approximately 40 min, and it may have been difficult for patients to remain still for this duration of time. Employing different accelerating techniques, such as stretching the readout trajectory, could be used to accelerate and optimize the 3D-UTE-Cones sequences, and limit the scans to 20 min with negligible resulted errors [42]. Another way to reduce the total scan time is to eliminate T1 mapping, which takes 20 min, about half of the total scan time. We are investigating bound and pore water T1s, especially their age dependence. Future *in vivo* studies may help generate an age-dependent table about bound and pore water T1s, which can then be used to interpolate values for mapping of desired proton densities. Alternatively, fewer number of proton densities may be selected for future clinical studies to reduce the scan time by focusing only on the parameters with highest correlations with bone porosity and mechanics. Third, the presented technique did not take fat presence in cortical bone into account, particularly in layers near the endosteum. The fat signal contribution may be similar to PW in the UTE-images [43], but the possibility of chemical shift impacting the estimated proton densities needs to be studied in a future investigation. Different fat suppression techniques, such as multi-echo acquisition with IDEAL [44], Dixon processing [45], or water excitation, could be an option for future studies. Fourth, bone mineral was not investigated in this study. Our prior studies suggest that 3D-UTE quantitative

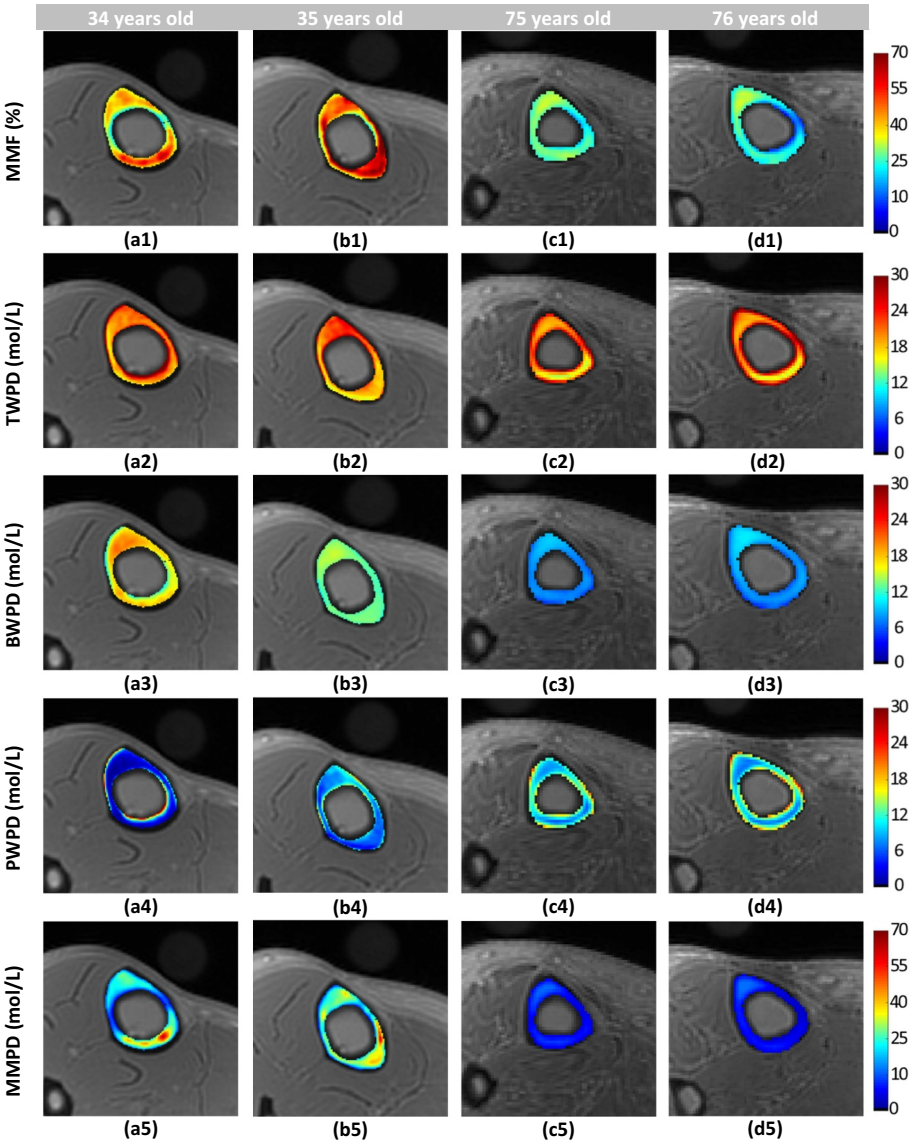

Fig. 6. Generated MMF and proton density maps for two young healthy volunteers, (a1-a5) 34-year-old female and (b1-b5) 35-year-old female, and two old volunteers, (c1-c5) 75-year-old female and (d1-d5) 76-year-old female. (a1-d1) MMF from 3D UTE-Cones-MT modeling. (a2-d2) Total water proton density (TWPD) maps from PD-weighted 3D UTE-Cones imaging. (a3-d3) Bound water proton density (BWPD) maps from 3D IR-UTE-Cones imaging. (a4-d4) Pore water proton density (PWPD) maps from the subtraction of TWPD from BWPD. (a5-d5) Macromolecular proton density (MMPD) maps from TWPD combined with MMF. In older individuals, PWPDs were higher, while BWPDs and MMPDs were lower compared with the younger group.

Table 2
Average proton densities from *ex vivo* (eight specimens, 63 ± 19 years old) and *in vivo* (ten young healthy and five old women) studies.

	TWPD (mol/L)	BWPD (mol/L)	PWPD (mol/L)	MMPD (mol/L)
Ex vivo	35.0 ± 3.2	16.0 ± 1.6	18.1 ± 2.4	44.7 ± 10.2
Young in vivo	29.3 ± 6.3	14.8 ± 2.2	14.8 ± 5.3	45.8 ± 12.4
Old in vivo	36.4 ± 8.3	13.0 ± 1.7	23.4 ± 8.7	29.8 ± 14.8

TWPD, BWPD, PWPD, and MMPD: total water, bound water, pore water, and macromolecular proton densities, respectively.

susceptibility mapping (3D-UTE-QSM) can be used to measure bone susceptibility, which is highly correlated with BMD. The addition of 3D-UTE-Cones-QSM to the current protocol may enable detection of all the components in cortical bone, including bound water, pore water, organic matrix, and bone mineral. Fifth, the proton density measurements are subject to partial volume artifact, which is more prominent in-plane than out-of-plane. The 3D UTE imaging slices were oriented perpendicular to the tibial midshaft, which is relatively homogenous along the long bone. The slice thickness of 2 mm (*ex vivo*) to 5 mm (*in vivo*) helps improve signal to noise ratio (SNR) in UTE imaging of bone and to minimize partial volume artifact in the slice direction. Partial voluming mainly comes from in-plane, due to limited in-plane resolution, short T2 blurring, and signal contamination from surrounding tissues. Partial volume artifact may be more significant in patients with thinner bone. Furthermore, partial volume artifact is greatly reduced in BWPD measurement where long T2 signals from muscle and marrow fat are well suppressed by the adiabatic inversion pulse. Future translational studies will be performed on the hip where 3D performance of the technique become crucial due to significant changes in the bone cross-sections. For future hip studies, specific interpolation or subvoxelization techniques are required to be added as a post-processing step to reduce the partial volume impacts.

5. Conclusion

A comprehensive protocol was presented to map proton densities as exist in water pools and bone matrix in cortical bone. MMPD mapping, based on recently developed two-pool UTE-MT modeling, was presented for the first time in the literature. MMPD represents proton density in collagenous bone matrix, which likely varies by aging and by bone injuries. Mapping proton densities was feasible for studied bone specimens and for volunteer subjects. Strong correlations between proton densities and bone microstructure, as measured with high resolution μCT, validated the presented technique for water proton

density measurement. As expected, PWPD showed the highest correlation with bone porosity. Strong correlation between MMPD and donor age, as well as significant differences between young and old *in vivo* groups, demonstrated the potential of this technique to assess age-related variations in bone matrix. The presented technique improved and extended the previously reported proton mapping in cortical bone. This technique can potentially serve as a novel tool to assess bone matrix and microstructure, as well as bone age- or injury-related variations in patients.

Declaration of Competing Interest

The authors have no conflicts of interest to declare.

Acknowledgements

The authors acknowledge grant support from NIH (1R21AR073496, R01AR068987, 1R01AR062581-01A1) and VA Clinical Science and Rehabilitation R&D Awards (I01CX001388 and I01RX002604).

Appendix I

- Total water proton density (TWPD)

TWPD in cortical bone can be estimated by comparing the UTE signal of cortical bone with that of the external reference [2, 5, 10, 20, 21, 24]. UTE signal can be estimated based on the Ernst equation, as presented in Eq. (1) [17].

$$SI_{Bone}(\mathrm{TE}) \propto \frac{1 - e^{-TR/T_{1-TW}}}{1 - \cos\theta \times e^{-TR/T_{1-TW}}} \times e^{-TE/T^{*}_{2-TW}} \times TWPD \tag{1}$$

where TR, θ, and $T_{1\text{-TW}}$ are repetition time, flip angle (FA), and total water longitudinal relaxation time, respectively. A proton density-weighted UTE acquisition can be used to simplify the calculation and minimize potential errors (*e.g.*, a relatively long TR of 100 ms, a short TE of 32 μs, and a low FA of 10° by using a short rectangular excitation pulse of 26 μs). Since $T2^*_{TW}$ and $T2^*_{REF}$ are much higher than TE and the rectangular excitation pulse duration, the T2* and T1 effects in Eq. (1) can be neglected; thus, the TWPD can be estimated using Eq. (2) by comparing the UTE signals of bone and external reference.

$$TWPD \approx \frac{SI^{UTE}_{Bone}}{SI^{UTE}_{REF}} \times \eta \times \rho_{REF} \tag{2}$$

where η and ρ_{REF} are coil sensitivity and proton density in the external reference, respectively. When TR is relatively short and FA is not small enough, Eq. (1) will be used for more accurate TWPD quantification.

- Bound water proton density (BWPD)

BWPD in cortical bone can be estimated by comparing the IR-UTE signal of cortical bone with that of the external reference [2, 5, 10, 20, 21, 24]. The IR-UTE signal can be estimated approximately with Eq. (3), with the assumption of complete saturation of BW, when the pore water nulling is efficient [17]. Thus, BWPD can be calculated using Eq. (4) by comparing the IR-UTE signals of bone and external reference when TE = 32 μs, $T2^*_{BW} \approx T2^*_{REF} \approx 350$ μs, and $T_{1\text{-REF}} \approx 6$ ms.

$$SI(t)_{IR-UTE} \propto (1 - e^{-TI/T_{1-BW}}) \times \sin\theta \times e^{-TE/T^{*}_{2}} \times BWPD \tag{3}$$

$$BWPD \approx \frac{SI^{IR-UTE}_{Bone}}{SI^{IR-UTE}_{REF}} \times \eta \times \rho_{REF} \times \frac{1}{1 - e^{-TI/T_{1-BW}}} \tag{4}$$

where $T_{1\text{-BW}}$ is bound water T_1.

- Pore water proton density (PWPD)

PWPD can be determined by subtracting BWPD from TWPD (Eq. (5)).

$$PWPD = TWPD - BWPD \tag{5}$$

- Macromolecular proton density (MMPD)

MMPD can be calculated using the two-pool MT modeling [27,33] combined with estimated TWPD (Eq. (2)). Two-pool MT modeling measures the macromolecular proton fraction, or MMF, which is the ratio between MMPD and all proton densities (TWPD + MMPD). Thus, MMPD can be calculated using Eq. (6).

$$MMPD = \frac{TWPD \times MMF}{1 - MMF} \tag{6}$$

Appendix II. Supplementary data, reproducibility study

Supplementary data to this article can be found online at https://doi.org/10.1016/j.bone.2019.05.038.

References

[1] E.Y. Chang, J. Du, C.B. Chung, UTE imaging in the musculoskeletal system, J. Magn. Reson. Imaging 41 (2015) 870–883, https://doi.org/10.1002/jmri.24713.
[2] J. Du, G.M. Bydder, Qualitative and quantitative ultrashort-TE MRI of cortical bone, NMR Biomed. 26 (2013) 489–506, https://doi.org/10.1002/nbm.2906.
[3] E.Y. Chang, J. Du, W.C. Bae, S. Statum, C.B. Chung, Effects of Achilles tendon

immersion in saline and perfluorochemicals on T2 and T2*, J. Magn. Reson. Imaging 40 (2014) 496–500, https://doi.org/10.1002/jmri.24360.
[4] C.S. Rajapakse, M. Bashoor-Zadeh, C. Li, W. Sun, A.C. Wright, F.W. Wehrli, Volumetric cortical bone porosity assessment with MR imaging: validation and clinical feasibility, Radiology 276 (2015) 526–535, https://doi.org/10.1148/radiol.15141850.
[5] A.C. Seifert, F.W. Wehrli, Solid-state quantitative 1H and 31P MRI of cortical bone in humans, Curr. Osteoporos. Rep. (2016) 1–10, https://doi.org/10.1007/s11914-016-0307-2.
[6] J.S. Nyman, Q. Ni, D.P. Nicolella, X. Wang, Measurements of mobile and bound water by nuclear magnetic resonance correlate with mechanical properties of bone, Bone 42 (2008) 193–199, https://doi.org/10.1016/j.bone.2007.09.049.
[7] J. Du, J.C. Hermida, E. Diaz, J. Corbeil, R. Znamirowski, D.D. D'Lima, G.M. Bydder, Assessment of cortical bone with clinical and ultrashort echo time sequences, Magn. Reson. Med. 70 (2013) 697–704, https://doi.org/10.1002/mrm.24497.
[8] M.K. Manhard, S. Uppuganti, M. Granke, D.F. Gochberg, J.S. Nyman, M.D. Does, MRI-derived bound and pore water concentrations as predictors of fracture resistance, Bone 87 (2016) 1–10, https://doi.org/10.1016/j.bone.2016.03.007.
[9] R.A. Horch, D.F. Gochberg, J.S. Nyman, M.D. Does, Non-invasive predictors of human cortical bone mechanical properties: T2-discriminated 1H NMR compared with high resolution X-ray, PLoS One 6 (2011) 1–5, https://doi.org/10.1371/journal.pone.0016359.
[10] M.K. Manhard, R.A. Horch, D.F. Gochberg, J.S. Nyman, M.D. Does, In vivo quantitative MR imaging of bound and pore water in cortical bone, Radiology 277 (2015) 221–230.
[11] S. Abbasi-Rad, H. Saligheh Rad, Quantification of human cortical bone bound and free water in vivo with ultrashort echo time MR imaging: a model-based approach, Radiology 000 (2017) 160780, , https://doi.org/10.1148/radiol.2016160780.
[12] M. Granke, A.J. Makowski, S. Uppuganti, M.D. Does, J.S. Nyman, Identifying novel clinical surrogates to assess human bone fracture toughness, J. Bone Miner. Res. 30 (2015) 1290–1300, https://doi.org/10.1002/jbmr.2452.
[13] W.C. Bae, P.C. Chen, C.B. Chung, K. Masuda, D. D'Lima, J. Du, Quantitative ultrashort echo time (UTE) MRI of human cortical bone: correlation with porosity and biomechanical properties, J. Bone Miner. Res. 27 (2012) 848–857, https://doi.org/10.1002/jbmr.1535.
[14] S. Jerban, Y. Ma, A. Nazaran, E.W. Dorthe, E. Cory, M. Carl, D. D'Lima, R.L. Sah, E.Y. Chang, J. Du, D. D'Lima, R.L. Sah, E.Y. Chang, J. Du, Detecting stress injury (fatigue fracture) in fibular cortical bone using quantitative ultrashort echo time-magnetization transfer (UTE-MT): an ex vivo study, NMR Biomed. 31 (2018) e3994, , https://doi.org/10.1002/nbm.3994.
[15] S. Jerban, Y. Ma, L. Wan, A.C. Searleman, H. Jang, R.L. Sah, E.Y. Chang, J. Du, Collagen proton fraction from ultrashort echo time magnetization transfer (UTE-MT) MRI modelling correlates significantly with cortical bone porosity measured with micro-computed tomography (μCT), NMR Biomed. 32 (2019) 1–10, https://doi.org/10.1002/nbm.4045.
[16] A. Techawiboonwong, H.K. Song, M.B. Leonard, F.W. Wehrli, Cortical bone water: in vivo quantification with ultrashort cortical bone water: in vivo quantification with ultrashort echo-time MR imaging, Radiology 248 (2008) 824–833.
[17] J. Du, M. Carl, M. Bydder, A. Takahashi, C.B. Chung, G.M. Bydder, Qualitative and quantitative ultrashort echo time (UTE) imaging of cortical bone, J. Magn. Reson. 207 (2010) 304–311, https://doi.org/10.1016/j.jmr.2010.09.013.
[18] H.S. Rad, S.C.B. Lam, J.F. Magland, H. Ong, C. Li, H.K. Song, J. Love, F.W. Wehrli, Quantifying cortical bone water in vivo by three-dimensional ultra-short echo-time MRI, NMR Biomed. 24 (2011) 855–864, https://doi.org/10.1002/nbm.1631.
[19] C. Li, A.C. Seifert, H.S. Rad, Y. a Bhagat, C.S. Rajapakse, W. Sun, S.C.B. Lam, F.W. Wehrli, Cortical bone water concentration: dependence of MR imaging measures on age and pore volume fraction, Radiology 272 (2014) 796–806, https://doi.org/10.1148/radiol.14132585.
[20] X. Zhao, H.K. Song, A.C. Seifert, C. Li, F.W. Wehrli, Feasibility of assessing bone matrix and mineral properties in vivo by combined solid state 1H and 31P MRI, PLoS One 12 (2017) 1–16, https://doi.org/10.1371/journal.pone.0173995.
[21] J. Du, A.J.T. Chiang, C.B. Chung, S. Statum, R. Znamirowski, A. Takahashi, G.M. Bydder, Orientational analysis of the Achilles tendon and enthesis using an ultrashort echo time spectroscopic imaging sequence, Magn. Reson. Imaging 28 (2010) 178–184, https://doi.org/10.1016/j.mri.2009.06.002.
[22] J. Chen, S.P. Grogan, H. Shao, D. D'Lima, G.M. Bydder, Z. Wu, J. Du, Evaluation of bound and pore water in cortical bone using ultrashort-TE MRI, NMR Biomed. 28 (2015) 1754–1762, https://doi.org/10.1002/nbm.3436.
[23] R.A. Horch, D.F. Gochberg, J.S. Nyman, M.D. Does, Clinically compatible MRI strategies for discriminating bound and pore water in cortical bone, Magn. Reson. Med. 68 (2012) 1774–1784, https://doi.org/10.1002/mrm.24186.
[24] M.K. Manhard, K.D. Harkins, D.F. Gochberg, J.S. Nyman, M.D. Does, 30-second bound and pore water concentration mapping of cortical bone using 2D UTE with optimized half-pulses, Magn. Reson. Med. 77 (2017) 945–950, https://doi.org/10.1002/mrm.26605.
[25] E.Y. Chang, W.C. Bae, H. Shao, R. Biswas, S. Li, J. Chen, S. Patil, R. Healey, D.D.D. Lima, C.B. Chung, J. Du, Ultrashort echo time magnetization transfer (UTE-MT) imaging of cortical bone, NMR Biomed. 28 (2015) 873–880, https://doi.org/10.1002/nbm.3316.
[26] Y. Ma, E.Y. Chang, M. Carl, J. Du, Quantitative magnetization transfer ultrashort echo time imaging using a time-efficient 3D multispoke Cones sequence, Magn. Reson. Med. 00 (2017) 1–9, https://doi.org/10.1002/mrm.26716.
[27] Y. Ma, H. Shao, J. Du, E.Y. Chang, Ultrashort echo time magnetization transfer (UTE-MT) imaging and modeling: magic angle independent biomarkers of tissue properties, NMR Biomed. 29 (2016) 1546–1552, https://doi.org/10.1002/nbm.3609.
[28] F. Springer, P. Martirosian, J. Machann, N.F. Schwenzer, C.D. Claussen, F. Schick, Magnetization transfer contrast imaging in bovine and human cortical bone applying an ultrashort echo time sequence at 3 Tesla, Magn. Reson. Med. 61 (2009) 1040–1048, https://doi.org/10.1002/mrm.21866.
[29] J. Chen, E.Y. Chang, M. Carl, Y. Ma, H. Shao, B. Chen, Z. Wu, J. Du, Measurement of bound and pore water T1 relaxation times in cortical bone using three-dimensional ultrashort echo time cones sequences, Magn. Reson. Med. 77 (2016) 2136–2145, https://doi.org/10.1002/mrm.26292.
[30] Y. Ma, X. Lu, M. Carl, Y. Zhu, N.M. Szeverenyi, G.M. Bydder, E.Y. Chang, J. Du, Accurate T 1 mapping of short T 2 tissues using a three-dimensional ultrashort echo time cones actual flip angle imaging-variable repetition time (3D UTE-Cones AFI-VTR) method, Magn. Reson. Med. 00 (2018) 1–11, https://doi.org/10.1002/mrm.27066.
[31] P.T. Gurney, B.A. Hargreaves, D.G. Nishimura, Design and analysis of a practical 3D cones trajectory, Magn. Reson. Med. 55 (2006) 575–582, https://doi.org/10.1002/mrm.20796.
[32] M. Carl, G.M. Bydder, J. Du, UTE imaging with simultaneous water and fat signal suppression using a time-efficient multispoke inversion recovery pulse sequence, Magn. Reson. Med. 76 (2015) 577–582, https://doi.org/10.1002/mrm.25823.
[33] Y. Ma, Y. Zhu, X. Lu, M. Carl, E.Y. Chang, J. Du, Short T 2 imaging using a 3D double adiabatic inversion recovery prepared ultrashort echo time cones (3D DIR-UTE-Cones) sequence, Magn. Reson. Med. 00 (2017) 1–9, https://doi.org/10.1002/mrm.26908.
[34] Y. Ma, A. Tadros, J. Du, E.Y. Chang, Quantitative two-dimensional ultrashort echo time magnetization transfer (2D UTE-MT) imaging of cortical bone, Magn. Reson. Med. (2017), https://doi.org/10.1002/mrm.26846.
[35] I.L.H. Reichert, M.D. Robson, P.D. Gatehouse, T. He, K.E. Chappell, J. Holmes, S. Girgis, G.M. Bydder, Magnetic resonance imaging of cortical bone with ultrashort TE pulse sequences, Magn. Reson. Imaging 23 (2005) 611–618, https://doi.org/10.1016/j.mri.2005.02.017.
[36] B. De Campos Vidal, M.L.S. Mello, Collagen type I amide I band infrared spectroscopy, Micron 42 (2011) 283–289, https://doi.org/10.1016/j.micron.2010.09.010.
[37] H.J. Butler, L. Ashton, B. Bird, G. Cinque, K. Curtis, J. Dorney, K. Esmonde-white, N.J. Fullwood, B. Gardner, P.L. Martin-Hirsch, M.J. Walsh, M.R. Mcainsh, N. Stone, F.L. Martin, Using Raman spectroscopy to characterise biological materials, Nat. Protoc. 11 (2016) 664–687, https://doi.org/10.1038/nprot.2016.036.
[38] K. Belbachir, R. Noreen, G. Gouspillou, C. Petibois, Collagen types analysis and differentiation by FTIR spectroscopy, Anal. Bioanal. Chem. 395 (2009) 829–837, https://doi.org/10.1007/s00216-009-3019-y.
[39] K. a Dooley, Raman Spectroscopic Studies of Bone Biomechanical by, (2011).
[40] Y. Wu, Y. Dong, J. Jiang, H. Li, T. Zhu, S. Chen, Evaluation of the bone-ligament and tendon insertions based on Raman spectrum and its PCA and CLS analysis, Sci. Rep. 7 (2017) 38706, , https://doi.org/10.1038/srep38706.
[41] A.L. Boskey, Bone composition: relationship to bone fragility and antiosteoporotic drug effects, Bonekey Rep. 2 (2013) 447, https://doi.org/10.1038/bonekey.2013.181.
[42] L. Wan, W. Zhao, Y. Ma, S. Jerban, A.C. Searleman, M. Carl, E.Y. Chang, G. Tang, J. Du, Fast quantitative three-dimensional ultrashort echo time (UTE) magnetic resonance imaging of cortical bone using extended cones sampling, Magn. Reson. Med. (2019), https://doi.org/10.1002/mrm.27715.
[43] X. Lu, S. Jerban, L. Wan, Y. Ma, H. Jang, N. Le, W. Yang, E.Y. Chang, J. Du, Three dimensional ultrashort echo time imaging with tri-component analysis for human cortical bone, Magn. Reson. Med. 00 (2019) 1–8, https://doi.org/10.1002/mrm.27718.
[44] C.S. Gee, J.T.K. Nguyen, C.J. Marquez, J. Heunis, A. Lai, C. Wyatt, M. Han, G. Kazakia, A.J. Burghardt, D.C. Karampinos, J. Carballido-Gamio, R. Krug, Validation of bone marrow fat quantification in the presence of trabecular bone using MRI, J. Magn. Reson. Imaging 42 (2015) 539–544, https://doi.org/10.1002/jmri.24795.
[45] H. Jang, M. Carl, Y. Ma, S. Jerban, T. Guo, W. Zhao, E.Y. Chang, J. Du, Fat suppression for ultrashort echo time imaging using a single point Dixon method, NMR Biomed. (2019) e4069, https://doi.org/10.1002/nbm.4069.